Separability of microtearing mode and electron temperature gradient turbulence regimes

E.A. Belli[1,*], J. Candy[1], I. Sfiligoi[2], and W. Guttenfelder[3]

[1] General Atomics, P.O. Box 85608, San Diego, CA 92186-5608, USA
[2] University of California San Diego, La Jolla, CA 92093 USA
[3] Type One Energy Group, Inc., Knoxville, TN 37931 USA

‡

E-mail: bellie@fusion.gat.com

Abstract. The separability of microtearing mode (MTM)-dominated and electron temperature gradient (ETG)-driven turbulence regimes is studied with multiscale nonlinear gyrokinetic simulations. The simulations are based on NSTX-like, high-confinement mode pedestal parameters, where electromagnetic perturbations are large. Linear analysis indicates a wide scale-separation between the MTM and ETG modes in binormal wavenumber space (perpendicular to the magnetic field line), with no unstable modes at intermediate scales. Likewise, single-scale nonlinear analyses, retaining ion-only or electron-only spatio-temporal scales, produce seemingly well-converged transport states. Surprisingly, the multiscale simulation, which contains both the ion and electron scales, closely follows the transport from the electron-scale simulation. This trend is robust over a wide range of electron temperature gradient. Remarkably, compared to ion-scale simulations, MTM turbulence is significantly reduced at multiscale resolution even when ETG turbulence is low. In this case, traditional ion-scale resolution overestimates the electron energy flux, and it is not possible to accurately simulate the MTM turbulence with separable ion-scale simulations. While the analysis confirms the validity of electron-scale simulations for predicting the electron transport, it also indicates that multiscale simulation may be required for reproducing the turbulence spectrum for systems with coupled MTM-ETG turbulence.

‡ *Author to whom any correspondence should be addressed.

1. Introduction

Accurate calculation of plasma turbulence in the high-confinement mode (H-mode) pedestal region of tokamak and spherical tokamak (ST) plasmas is critical for design and conceptual validation of future fusion reactors. Compared to conventional tokamaks, STs like the National Spherical Torus Experiment (NSTX) operate at high plasma β (the ratio of the plasma thermal pressure to the magnetic pressure). As a result, electromagnetic drift-wave instabilities, such as microtearing modes (MTMs) and kinetic ballooning modes (KBMs), may dominate over electrostatic instabilities at long (ion-gyroradius-scale) wavelengths [1, 2, 3]. This is in contrast to conventional tokamaks where electrostatic instabilities such as the ion temperature gradient (ITG) mode and trapped electron mode (TEM) often dominate. However, electromagnetic instabilities are expected to be more important in advanced tokamaks (ATs) with relatively high β and large self-generated bootstrap current [4].

In the H-mode pedestal, electrostatic instabilities are often suppressed by strong $\mathbf{E} \times \mathbf{B}$ sheared flows, apparently reducing the ion energy transport to neoclassical levels [5, 6] such that electron transport is dominant. Gyrokinetic analysis has indicated that, at short (electron-gyroradius-scale) wavelengths, electron temperature gradient (ETG)-driven modes are often unstable due to the steep pedestal temperature and density gradients [7, 8, 9, 10]. Thus, ETG modes are believed to be a dominant driver of pedestal electron transport. Recent simulations have also suggested that MTM turbulence may provide an additional source of the pedestal electron transport in tokamak experiments [11, 12, 9]. Studies of nonlinear MTM turbulence in STs have mostly been limited to core regions [2, 13, 3, 14] since electromagnetic field stochasticity and proximity to KBM stability boundaries in the pedestal make nonlinear simulation more difficult [15, 16, 17].

In all cases, simulations are overwhelmingly based on single-scale analysis, i.e. resolving only *ion scales* (wavelengths perpendicular to the magnetic field line that are equal to or longer than the ion gyroradius) or resolving only *electron scales* (wavelengths perpendicular to the magnetic field line that are smaller than the ion gyroradius and on the order of the electron gyroradius). Multiscale simulations, covering the full wavenumber and timescale range, are far more computationally challenging, requiring leadership-scale computing resources. Previous multiscale simulation has focused mainly on the conventional tokamak core and the interaction of ITG and ETG turbulence [18, 19, 20, 21] (see also review of multiscale turbulence studies in [22] and references therein). In fact, only recently have multiscale simulations of tokamak pedestal turbulence been performed [23, 24], demonstrating that experiments can lie in a bifurcation region between ion-scale-dominated transport and multiscale transport. These results suggest that pedestal turbulence may often be multiscale.

Multiscale simulation of MTM and ETG turbulence has been even less well-studied. A first demonstration [25], based on ASDEX-Upgrade parameters at mid-core, started with a saturated ion-scale simulation of MTM turbulence, refining the numerical grid to include electron scales, and then running for several ion thermal timescales. This work importantly showed that the MTM-driven turbulence was suppressed – apparently by ETG turbulence. In the present work, through the use of exascale computing resources, we expand on this result by using multiscale gyrokinetic simulations to study the cross-scale interaction between MTM and ETG turbulence for parameters characteristic of an NSTX pedestal. Parameter scans, varying the electron temperature gradient, are performed to vary the conditions under which ETG or MTM-driven turbulence is expected to dominate. Long-time simulations (to several hundred ion thermal timescales) ensure that long-wavelength fluctuations and long-wavelength zonal flows can reach a statistical steady state, and that their effect on the electron-scale modes is physically correct.

Since most pedestal modeling (in both tokamaks and STs) and MTM modeling (in both the core and pedestal) is performed with single-scale analysis, a strong motivation for this work is to explore the validity of the so-called *separability approximation*. This approximation amounts to an assumption that ion-scale turbulence and electron-scale turbulence can be computed separately and then added to compute the total flux, thereby eliminating the need for expensive multiscale coupling. In this work, we study the separability of ion-scale MTM turbulence from electron-scale ETG turbulence.

The remainder of this paper is organized as follows. In Section 2, the basis of the separability approximation is explained. Section 3 outlines the baseline NSTX-like pedestal simulation parameters, and Section 4 defines the single-scale and multiscale numerical resolutions. The linear eigenmode analysis, defining the regions of wavenumber space where MTM and ETG-driven turbulence are expected, is detailed in Section 5. Section 6 presents the analysis of high-fidelity multiscale simulation of coupled MTM-ETG turbulence. Comparisons are made with standard, single-scale simulations to assess the validity of the separability approximation. Finally, a summary is given in Section 7.

2. Separability approximation for ion-scale and electron-scale turbulence

To avoid the high computational expense of multiscale coupling, gyrokinetic analysis is normally done at a single scale and relies on the validity of the separability approximation. The approximation is based on two assumptions. The first is that the ion-scale and electron-scale components of the fluxes are *calculable* by separate ion-gyroradius-scale and electron-gyroradius-scale simulations. Mostly this implies that the separate simulations converge numerically, producing a saturated transport state. For example, in some electron-scale simulations, lack of long-wavelength zonal flows can result in runaway (non-saturation) of the transport. The second assumption is that the components of the fluxes from single-scale simulations are *additive* in such a way that the sum reproduces the result from the more comprehensive multiscale simulation. This implies that there are no significant cross-scale or intermediate-scale interactions between the turbulent perturbations in perpendicular wavenumber space. Because of the limited number of multiscale simulations, it is not clear when separable simulations are valid as a proxy for a multiscale system. This uncertainty extends to pedestal regions, where ion-scale turbulent transport is often suppressed by $\mathbf{E}\times\mathbf{B}$ shear and/or there are no unstable modes at intermediate wavelengths. The only true test of the validity of the separability approximation is to perform a simulation with full multiscale resolution. Identification of specific regimes where the approximation works is the first step toward understanding more generally when multiscale simulation is required and when single-scale simulation may be sufficient.

3. Baseline pedestal simulation parameters

The simulations in this study are based on H-mode, pedestal-like parameters from NSTX discharge #132588 at $t = 650$ ms [26]. This experiment demonstrated access to a very wide pedestal and an enhanced performance regime that was free of edge-localized modes (ELMs) due to reduced neutral recycling via lithium wall conditioning. We consider a radial location in the steep-gradient region at $r/a = 0.9$ (normalized poloidal flux $\psi_N = 0.87$). Previous analysis suggested that the electron transport from nonlinear gyrokinetic ETG turbulence (via electron-scale simulation) plus ion neoclassical transport can account for roughly 50% of the total target experimental energy flux [27]. Global linear analysis has also identified unstable MTMs [28]. The purpose of the present study is not to perform an extensive experimental analysis of pedestal transport, but rather to evaluate the cross-scale interactions of MTM and ETG turbulence in this type of scenario.

For these studies, we use the gyrokinetic code CGYRO [29, 30, 31] to compute the turbulent transport. Simulations were performed in the local, flux-tube limit. Equilibrium parameters are given in Appendix A. For simplicity, impurities are neglected. Shaped flux-surface geometry [32] (not up-down symmetric) is used, and multi-species collisions are included using the Sugama collision operator [33]. Rotation (equilibrium $\mathbf{E}\times\mathbf{B}$ flow shear) is also included. Importantly, transverse electromagnetic fluctuations ($\delta A_\parallel$) are retained, but compressional magnetic field fluctuations ($\delta B_\parallel$) are neglected in the simulations to eliminate closeness to the KBM stability limit. It was confirmed that the growth rate of the MTM is quantitatively similar when neglecting $\delta B_\parallel$, but the KBM is suppressed. Finally, the inverse electron temperature gradient scale length, $1/L_{Te} \doteq -d\ln T_e/dr$, which is a key driving parameter for electron turbulence, is varied around the baseline experimental value to mimic the transition from MTM-dominant to ETG-dominant turbulence.

In what follows, energy fluxes are normalized by the gyroBohm reference level $Q_{\rm GB} \doteq n_e T_e c_s \rho_*^2$, where n_e is the electron density, T_e is the electron temperature, $c_s = \sqrt{T_e/m_D}$ is the deuteron sound speed, and $\rho_* = \rho_s/a$ is the ratio of the deuteron sound gyroradius $\rho_s = c_s/\Omega_{c,\rm unit}$ to the system size. Here, m_D is the deuteron mass, a is the midplane minor radius of the last closed flux surface, and $\Omega_{c,\rm unit} = eB_{\rm unit}/(m_D c)$ with $B_{\rm unit}(r) = (q/r)(d\psi/dr)$, defined with respect to q (safety factor), and ψ (poloidal flux divided by 2π) [34]. The equivalent experimental flux from power-balance analysis (often called the target flux) is $Q^{\rm exp}_{\rm total}/Q_{\rm GB} = 48$. For reference, the neoclassical energy fluxes from the NEO code [35, 36] for the full case (including carbon impurities) are $Q_i^{\rm neo}/Q_{\rm GB} = 18$ and $Q_e^{\rm neo}/Q_{\rm GB} = 1.3$. In the simplified case, this is reduced to $Q_i^{\rm neo}/Q_{\rm GB} = 8.6$ and $Q_e^{\rm neo}/Q_{\rm GB} = 0.8$. However, it is still expected that the ion energy transport is dominantly neoclassical, i.e. the turbulent ion energy transport is relatively negligible. This will be confirmed in what follows.

4. Single-scale vs. multiscale numerical resolution

We consider a baseline multiscale resolution with corresponding single-scale (ion-scale only and electron-scale only) resolutions in order to assess separability. We will refer to simulations using these as MULTI, I-SCALE and E-SCALE, respectively. The detailed numerical resolution parameters are defined in Table 1. The multiscale simulations use a radial box length of $L_x = 146\rho_s$ and a binormal box length of $L_y = 349\rho_s$. $N_r = 1152$ radial modes and $N_\alpha = 768$ complex toroidal modes are retained. These resolutions were determined based on radial and binormal box size convergence for the ion-scale simulations [varying L_x and L_y at fixed $(k_x^0\rho_s)_{\max}$ and $(k_\theta\rho_s)_{\max}$]. Note that these are among the largest spatially-resolved simulations reported to date. The total ensemble of five full multiscale resolution simulations required 250k node-hours on the *exascale*

Table 1. Multiscale, ion-scale, and electron-scale numerical resolution definitions for the radial (L_x) and binormal (L_y) box sizes, number of wavenumbers in each dimension (N_r and N_α), and corresponding minimum and maximum wavenumbers.

	L_x	$\Delta(k_x^0\rho_s)$	$(k_x^0\rho_s)_{\max}$	N_r	L_y	$\Delta(k_\theta\rho_s)$	$(k_\theta\rho_s)_{\max}$	N_α
MULTI	$146\rho_s$	0.043	24.7	1152	$349\rho_s$	0.018	13.8	768
I-SCALE	$146\rho_s$	0.043	4.1	192	$349\rho_s$	0.018	0.85	48
E-SCALE	$4.0\rho_s$	1.57	25.1	34	$4.1\rho_s$	1.53	13.8	10

Frontier supercomputer at the Oak Ridge Leadership Computing Facility (OLCF). The ion-scale simulations use the same box sizes, but resolve only low perpendicular wavenumbers relevant for ion dynamics. However, we will show that for this case it is necessary to use very high radial resolution [up to the multiscale $(k_x^0\rho_s)_{\max}$] for convergence of the MTM, as lower radial resolution results in spurious transport. The electron-scale simulations, on the other hand, neglect ion-gyroradius scales, resolving only high $k_\perp$, on the order of the inverse electron gyroradius. Specifically, the electron-scale simulations resolve up to the same maximum wavenumbers as the multiscale simulations but use much smaller box sizes. Finally, other resolution parameters (for multiscale, ion-scale, and electron-scale simulation) are $N_\theta = 48$ (field line resolution), $N_\xi = 18$ (pitch-angle resolution), and $N_u = 8$ (energy resolution) with maximum energy $u^2_{\max} = 8$, same as for the linear simulations. For reference, explicit definitions of the CGYRO numerical resolution parameters can be found in [29].

5. Separability in linear wavenumber spectrum

The linear eigenmode analysis is shown in Fig. 1 for a range of a/L_{Te}. The results are shown for two different values of the ballooning parameter θ_0 [37, 38], where $\theta_0 \in [-\pi, \pi)$. Linear microinstabilities typically peak at $\theta_0 = 0$. However, it has been shown that modes that peak at finite θ_0 can be destabilized in steep-gradient regions like the pedestal, with growth rates that are higher than the mode at $\theta_0 = 0$ [39, 40, 41]. For the modes in Fig. 1, it was confirmed that all unstable modes are in the electron diamagnetic direction. An MTM is the dominant mode at low k_θ. The mode structure for the MTM exhibits an odd (so-called *tearing*) parity for the fluctuating electrostatic potential $\delta\phi$ and an even parity for the fluctuating transverse electromagnetic potential $\delta A_\parallel$, as shown in Fig. 2. This is a characteristic feature of MTMs. For the MTM, the electromagnetic fluctuations are relatively large, with $(\mathrm{v_e}/\mathrm{c_s})\left|\delta \mathrm{A}_\parallel\right| > |\delta\phi|$. We use the factor of the electron thermal speed $\mathrm{v_e}$ to emphasize that this term is dominant in the electron equation [42]. In Fig. 1, there are notably no unstable modes at intermediate wavenumbers, specifically in the range of $0.4 < k_\theta\rho_s < 2.5$. ETG modes dominate at high k_θ. At the low end of the region where ETG modes are unstable, the dominant ETG mode is not peaked at $\theta_0 = 0$. The dependence of the linear growth rate on θ_0 at $k_\theta\rho_s = 13.8$ is shown in Fig. 3. The result for $k_\theta\rho_s = 0.2$ is also shown for comparison. At both wavenumbers, multiple modes are unstable. At the lower wavenumber, the dominant mode is localized around $\theta_0 = 0$. At the higher wavenumber, two ETG modes are unstable, one localized around $\theta_0 = 0$ and one localized around $\theta_0 = 0.035$. While the value of θ_0 at the peak for the latter mode varies somewhat with k_θ, we have found the variation of the maximum linear growth over θ_0 at a particular k_θ for this mode to be weak. Thus, in Fig. 3, we show only the case of $\theta_0 = 0.035$ as an estimation for the linear stability of this mode. As shown in Fig. 4, both of the ETG modes have even parity for $\delta\phi$ (shifted for the finite-θ_0 mode), in contrast to the MTM. The electomagnetic fluctuations are relatively small ($\left|\delta A_\parallel\right| \ll |\delta\phi|$) and the nonlinear turbulence is expected to be electrostatic-driven.

The electron temperature gradient can provide a source of free energy for both MTMs and ETGs. In the parameters we consider, the variation of the linear growth rate of the MTM with a/L_{Te} is non-monotonic but weak. However, the width of the instability range in wavenumber narrows as a/L_{Te} increases, and the linear growth rate peaks at smaller k_θ, such that $\left[\left(\gamma a/c_s\right)/\left(k_\theta \rho_s\right)\right]_{\text{peak}}$ monotonically increases from $a/L_{Te} = 10$ to $a/L_{Te} = 27.5$. This indicates that larger electron transport from low-k_θ fluctuations may be expected at larger a/L_{Te}. At small scales, the linear growth rate of the ETG modes increases strongly with increasing a/L_{Te} as expected. For the electron-scale range, there are multiple unstable ETG modes, including a mode that persists up to $k_\theta \rho_e \sim 5$. Further investigation shows that this is a slab mode sensitive to geometry; in particular, the mode is suppressed for Shafranov shift $dR_0/dr \gtrsim -0.2$. Nevertheless, due to computational limitations, it is not feasible to explore the full range of unstable ETG modes, and thus we will restrict our nonlinear analysis to ETG modes in the range of $k_\theta \rho_i < 15$ (i.e. neglecting the gray region in Fig. 1). For each case, $\left[\left(\gamma a/c_s\right)/\left(k_\theta \rho_s\right)\right]_{\text{peak}}$ for the ETG modes with $\theta_0 = 0$ in this range is less than the value for the MTM, even for the case of $a/L_{Te} = 27.5$. This is also the case for the finite-θ_0 mode for $a/L_{Te} < 17.3$. For coexisting ITG and ETG turbulence, it has been shown for some limited cases that the relation of this ratio for an ITG mode vs. an ETG mode may be used as a measure of the validity of the separability approximation [43, 44]. Specifically, if the ratio is greater than 1, then cross-scale coupling in multiscale transport may not be important, and ion-scale ITG simulation may reproduce the multiscale transport. This of course assumes that the single-scale simulations converge. It is unclear if this measure can be applied to systems with MTMs.

Finally, the linear wavenumber spectrum in Fig. 1 suggests that a separability of regimes of MTM turbulence and ETG turbulence may exist, without any cross-scale interaction, since there are no unstable drift modes in the intermediate wavenumber range. Linear analysis shows that the primary source of separability is the density gradient. For example, as shown in Fig. 5 for the $\theta_0 = 0$ mode, as a/L_n decreases, both the MTM and ETG are destabilized over a wider range of wavenumbers. However, we do not vary density gradient in this work because the MTM growth rate quickly rises to very high (potentially unphysical) levels.

6. Multiscale analysis of coupled MTM-ETG turbulence

Results from nonlinear multiscale simulations are analyzed in a scan over a/L_{Te}. Comparisons are made with single-scale nonlinear simulations (i.e. ion-scale and electron-scale as defined by the resolution parameters in Table 1) with the ultimate goal of assessing validity of the separability approximation. In what follows, we will establish several key results as summarized below:

- Both single-scale simulations (ion-scale MTM and electron-scale ETG) converge numerically, yielding plausible steady states of turbulence.

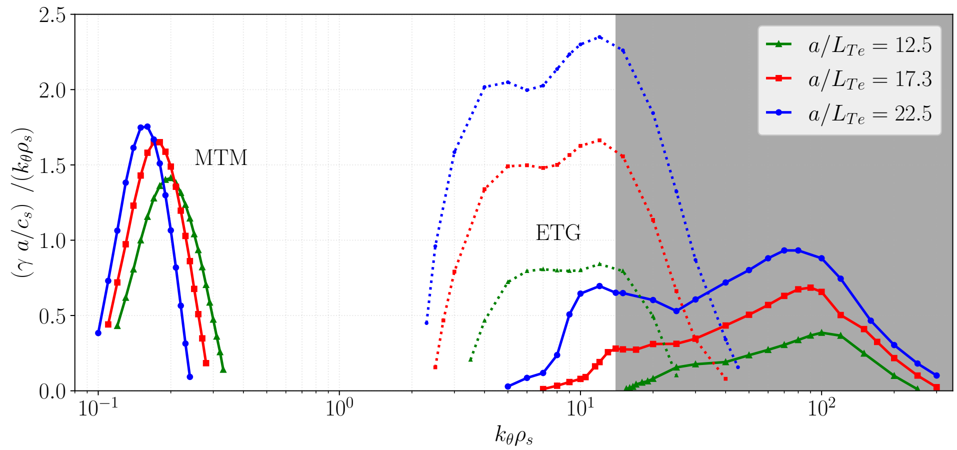

Figure 1. Linear growth rate versus $k_\theta \rho_s$ for a range of a/L_{Te}. Solid lines correspond to $\theta_0 = 0$, while dotted lines correspond to $\theta_0/(2\pi) = 0.035$. At low wavenumbers an MTM is dominant, while at high wavenumbers ETG modes dominate. The spectrum is separable in that no modes are linearly unstable at intermediate wavenumbers $0.4 \leq k_\theta \rho_s \leq 2.5$. Note that, in the nonlinear simulations, the gray region is neglected.

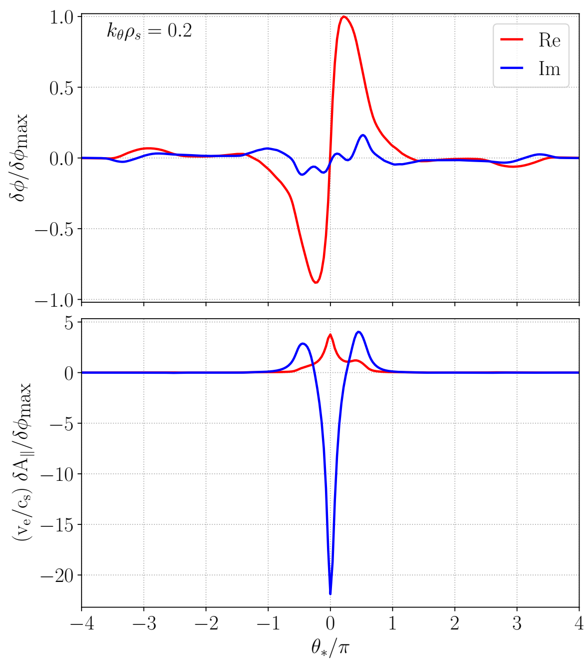

Figure 2. Linear eigenmodes for the MTM at $k_\theta \rho_s = 0.2$ for the case of $a/L_{Te} = 17.3$. The MTM has characteristic odd parity for $\delta\phi$, which is also extended in ballooning angle, and has relatively large electromagnetic fluctuations, i.e. $(\mathrm{v_e}/\mathrm{c_s}) \left|\delta \mathrm{A}_\parallel\right| > |\delta\phi|$.

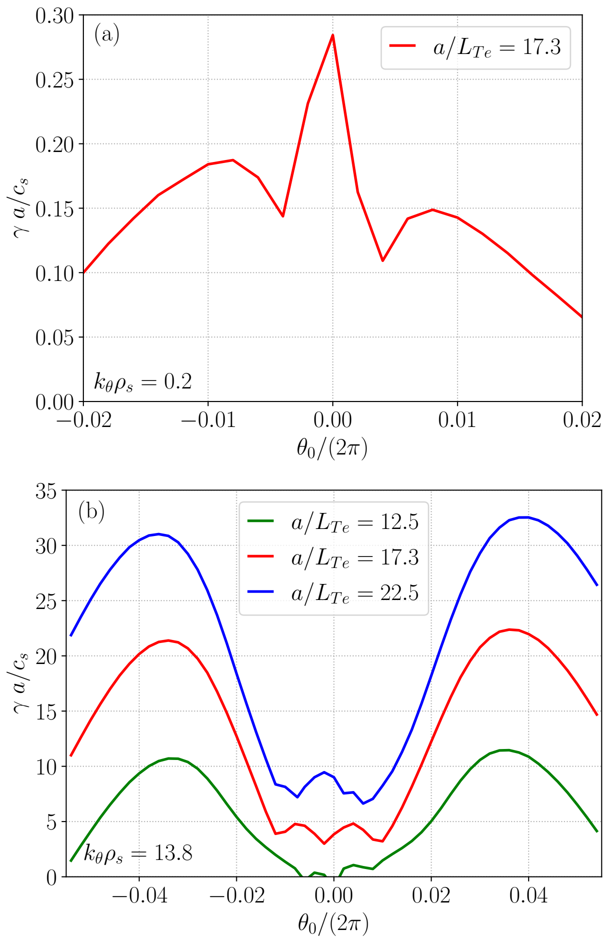

Figure 3. Linear growth rate versus ballooning parameter θ_0 for a range of a/L_{Te} at (a) $k_\theta\rho_s = 0.2$ and (b) $k_\theta\rho_s = 13.8$. At the lower wavenumber, the dominant mode is localized around $\theta_0 = 0$. At the higher wavenumer, the mode localized around a peak of $\theta_0/(2\pi) = 0.035$ has larger maximum growth rate than the mode localized at $\theta_0 = 0$.

- Saturation of electron fluxes in electron-scale simulations is due to a combination of short-wavelength zonal-nonzonal mode coupling and nonzonal-nonzonal mode coupling in the absence of ion-scale zonal flows.
- Multiscale fluxes are nearly equal to electron-scale fluxes, implying a suppression of ion-scale MTM turbulence.
- MTM turbulence is significantly reduced in multiscale simulations even when high-k_θ turbulence is low, so cannot be attributed to ETG-coupling.
- Traditional ion-scale simulations generate spurious MTM-driven transport that significantly overestimates Q_e. Numerical convergence of ion-scale simulations requires *multiscale* radial resolution. However, even then, it is not possible to fully reproduce the ion-scale transport observed in the multiscale simulation. Nonlinear coupling to high-k_θ modes is non-trivial.

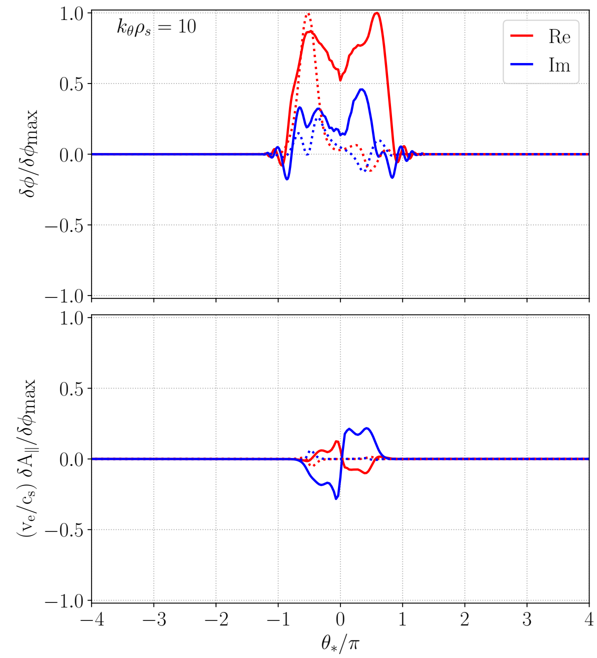

Figure 4. Linear eigenmodes for ETG modes at $k_\theta \rho_s = 10$ for the case of $a/L_{Te} = 17.3$. Solid lines correspond to $\theta_0 = 0$, while dotted lines correspond to $\theta_0/(2\pi) = 0.035$. Both modes have even parity for $\delta\phi$ (shifted for the finite-θ_0 mode) and relatively small electromagnetic fluctuations ($|\delta A_\parallel| \ll |\delta\phi|$).

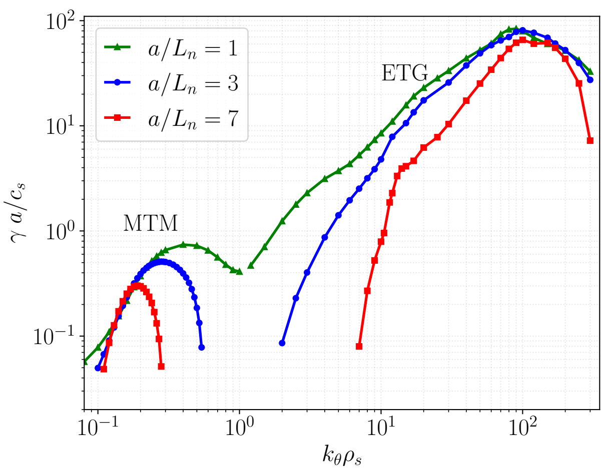

Figure 5. Linear growth rate versus $k_\theta \rho_s$ for a range of inverse density gradient scale lengths a/L_n for the case of $a/L_{Te} = 17.3$. Only modes with $\theta_0 = 0$ are shown. At low wavenumbers an MTM is dominant, while at high wavenumbers ETG modes dominate. As a/L_n decreases, both the MTM and ETG are destabilized over a wider range of wavenumbers, such that the apparent separability of the two regimes closes.

- In this case, multiscale simulations confirm the validity of electron-scale simulations for predicting electron transport. However, the MTM-driven transport with separable ion-scale simulations, while small, is not valid. Multiscale resolution is required to recover the correct ion-scale turbulence spectrum.

To begin the analysis, Fig. 6 shows the results for the multiscale electron and ion energy fluxes. For all values of a/L_{Te}, the electron energy flux is larger than the ion flux. The ion energy transport is dominantly neoclassical, as expected. It was confirmed that the fluxes are electrostatic-driven, such that the electromagnetic component is more than an order of magnitude smaller. The fluctuations of the electrostatic and electromagnetic potentials for the multiscale turbulence are shown in Fig. 7. The eddies of the electrostatic fluctuations are characterized by short (electron) scales. In contrast, the electromagnetic fluctuations have large (ion-scale) radial correlation lengths, although these are much smaller in amplitude. Overall, these results imply that the multiscale transport is dominated by ETG-driven turbulence.

In Fig. 6, comparisons are made with the electron-scale (ETG) simulations. Surprisingly, the electron-scale simulations not only converge, exhibiting a saturated state to long times ($t > 100a/c_s$), but the electron-scale energy fluxes also very closely follow the multiscale fluxes. At first glance, these results imply suppression of MTM turbulence by ETG turbulence, as indicated in the results of Ref. [25]. The electron fluxes from both the multiscale and electron-scale simulations increase as a/L_{Te} increases, consistent with the linear ETG drive in Fig. 1. Relatedly, we also find that the multiscale fluxes are suppressed for $a/L_{Te} \lesssim 10$. At this gradient, the ETG mode at $\theta_0 = 0$ is stable and the mode at $\theta_0 = 0.035$ is only weakly unstable, with $[(\gamma a/c_s)/(k_\theta \rho_s)]_{\text{peak}} = 0.355$ and the region of instability limited to $4.5 \lesssim k_\theta \rho_s \lesssim 20$. On the other hand, the MTM remains unstable. This means that the suppression (to a low level) of MTM-driven turbulence in this case is *unlikely* to be attributed to coupling with ETG-driven turbulence.

To explore the multiscale temporal dynamics, we plot time traces at $a/L_{Te} = 17.3$ in Fig. 8. The plot compares the ion-scale component of Q_e (i.e. summing over binormal wavenumbers $k_\theta \rho_s < 1$) to the component consisting of the intermediate through electron scales ($k_\theta \rho_s > 1$). At times shorter that the ion timescale ($t < 1a/c_s$), the turbulence is dominated by high-k_θ (ETG) modes. In this plot, it is clear that the MTM-driven turbulence is indeed present and not fully suppressed, as the linear MTMs at ion-scale wavenumbers begin to grow around $t \sim 10a/c_s$ with saturation reached by $t \sim 100a/c_s$. There is a finite but small contribution of the low-k_θ turbulence to the electron flux.

The zonal electrostatic potential intensity is also shown in Fig. 8. We define this as

$$I^{(0)} = \sum_{k_x^0} \left\langle \left| \hat{\phi}(k_\theta = 0, k_x^0) \right|^2 \right\rangle_t , \tag{1}$$

where $\langle \cdots \rangle_t$ denotes a time-average and $\hat{\phi} \doteq e\delta\phi/T_e$. The multiscale zonal intensity grows on the ion timescale, following the increasing $Q_e^{k_\theta<1}$. This is consistent with the usual case for ITG turbulence that zonal flows are dominantly driven by low-k_θ modes; though, in this case, they are driven by the MTMs. Unlike previous short-time multiscale simulations, these were run well into ion timescales, confirming that we do not observe any stabilizing effect of the low-k_θ MTMs on the high-k_θ ETG

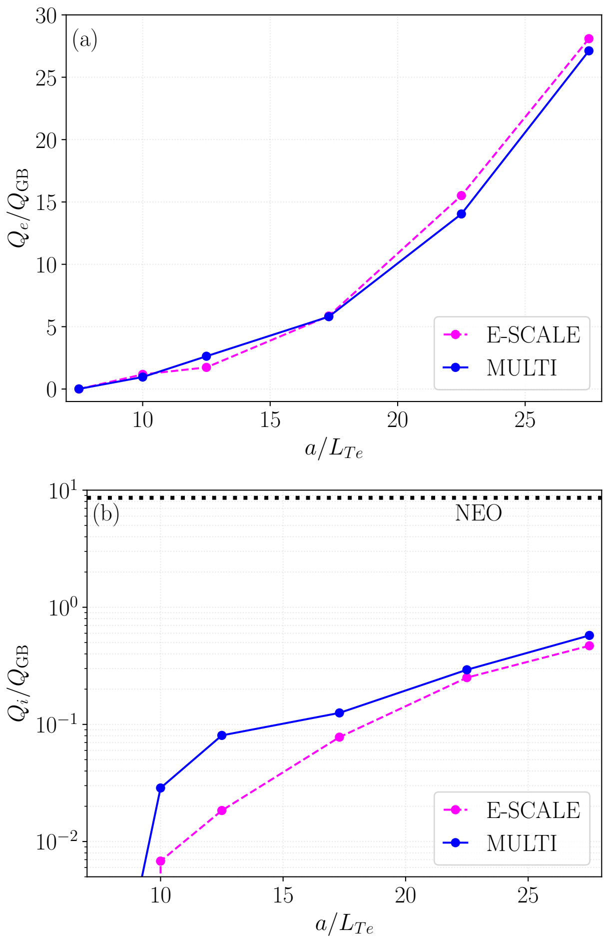

Figure 6. (a) Electron and (b) ion energy fluxes versus a/L_{Te}. Simulation results at electron-scale resolution (E-SCALE) are compared with multiscale resolution (MULTI). The multiscale fluxes follow the electron-scale fluxes. The turbulent Q_i is small and much lower than the neoclassical flux (NEO).

transport. This is consistent with the matching of the electron-scale transport fluxes with the multiscale fluxes. That the ETG turbulence here is largely unaffected by the ion-scale turbulence is in contrast to prior multiscale simulation of coupled ITG-ETG turbulence, where high-k_θ turbulence is reduced by nonlinear coupling to low-k_θ modes and ion-scale zonal flows [18, 19, 20]. This is also in contrast to prior simulations which showed a suppression of electron-scale flux by MTM-driven zonal flows [45].

To further investigate the scale-separation dynamics, we analyze the nonlinear wavenumber spectra. We define the spectral density of energy flux $\tilde{Q}_a$ for species a in terms of the total flux as

$$Q_a = \sum_k \Delta k \, \tilde{Q}_a^k \, , \tag{2}$$

where $k \doteq k_\theta \rho_s$. The spectral density for the electron energy flux is shown in Fig. 9 for various a/L_{Te} for the multiscale simulations. The plots are separated to highlight

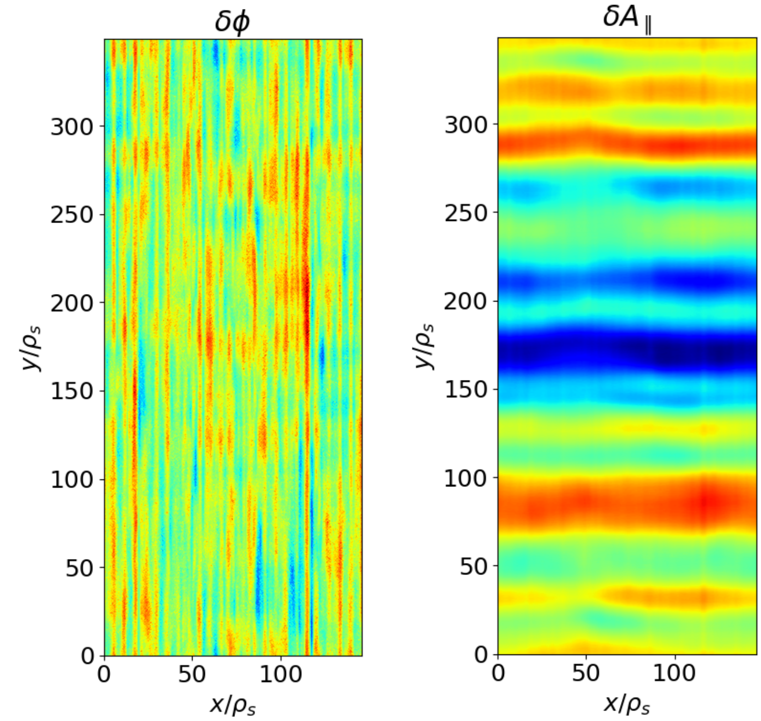

Figure 7. Multiscale fluctuations of the electrostatic potential $\delta\phi$ and electromagnetic potential $\delta A_\parallel$ for the case of $a/L_{Te} = 17.3$. The eddies of the electrostatic fluctuations are characterized by short (electron) scales, while the electromagnetic fluctuations have large (ion-scale) radial correlation lengths.

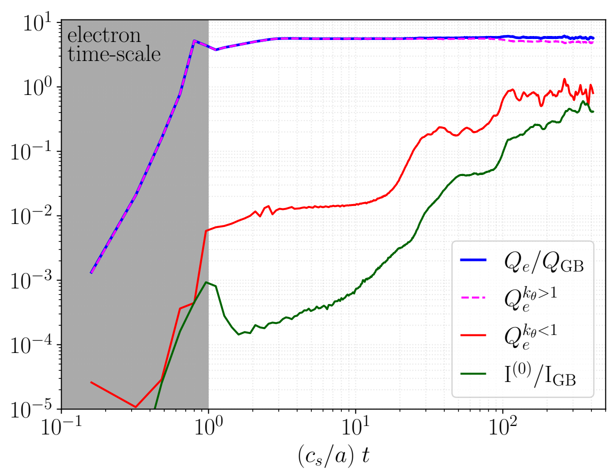

Figure 8. Time trace of multiscale electron energy flux Q_e for $a/L_{Te} = 17.3$. The sub-components of the flux containing low (ion-scale, $k_\theta\rho_s < 1$) and high ($k_\theta\rho_s > 1$) wavenumbers are shown. The high wavenumber range dominates the total flux, even though the zonal electrostatic potential intensity I_0 increases as the ion-scale transport grows.

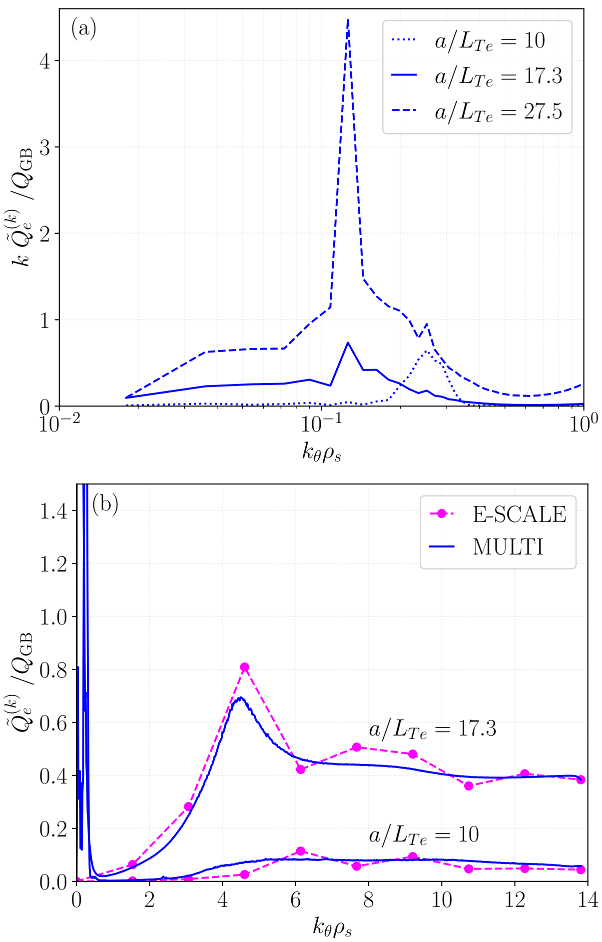

Figure 9. Spectral density of the electron energy flux $Q_e^{(k)}$ as a function of binormal wavenumber for multiscale simulation at various a/L_{Te}, comparing (a) the ion-scale spectra and (b) the electron-scale spectra. The area under the curve is the total flux. The spectra for the reduced, electron-scale resolution simulation (E-SCALE) closely matches the full multiscale simulation.

the ion-scale and electron-scale binormal wavenumber spectra, such that the area under the curve represents the total flux. It is clear that the low wavenumbers do not contribute significantly to the overall transport due to extreme localization in wavenumber space. The localization qualitatively corresponds with the region of unstable MTM linear modes in Fig. 1. In contrast, at higher wavenumbers the turbulence shows a relatively broad spectrum. This is qualitatively consistent with the range of linear instability for the finite-θ_0 ETG mode in Fig. 1. Importantly, the spectral density for the multiscale simulation closely matches that of the electron-scale simulation, confirming not only dominance of ETG-driven turbulence but also validity of the electron-scale simulation for accurately modeling the electron transport channel.

Since the electron-scale simulation does not couple to ion-scale zonal and non-zonal modes, an alternative mechanism must be responsible for saturation of the high-

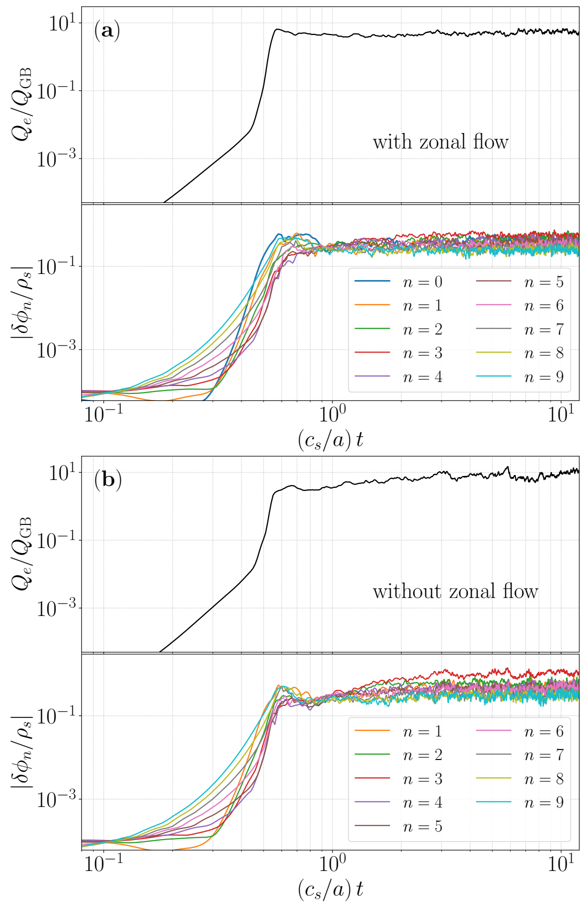

Figure 10. Illustration of the effect of removing the zonal flow coupling. Plot (a) shows short-time E-SCALE simulation, producing $Q_e/Q_{\mathrm{GB}} = 5.55$. In plot (b), the $n = 0$ zonal response has been decoupled nonlinearly from the gyrokinetic equation, causing the flux to increase to $Q_e/Q_{\mathrm{GB}} = 9.86$. Thus with nonzonal mode-mode coupling only, the saturation level increases by a factor of 1.8. This suggests that zonal-nonzonal mode coupling has about the same importance as nonzonal-nonzonal mode coupling in setting the saturation amplitude.

k_θ turbulence and related numerical convergence of the electron-scale simulations. To further understand the role of zonal flows, we performed electron-scale simulations decoupling the zonal ($k_\theta = 0$) response nonlinearly from the gyrokinetic equation, leaving only nonzonal mode-mode coupling. The results are shown in Fig. 10. Here, the fluxes still saturate *without* nonlinear coupling to short-wavelength zonal flows, but at a somewhat higher level (1.8× the original flux). Thus both zonal-nonzonal and nonzonal-nonzonal coupling play comparable roles in setting the saturation level.

Finally, we revisit the validity of the ion-scale MTM simulation. Determining the proper radial resolution for nonlinear gyrokinetic simulations is non-trivial. Compared with core parameters, large magnetic shear in the pedestal reduces the natural periodicity length L of the mode according to $L = 1/(sk_\theta)$, as in Eq. (76) of Ref. [29]. Equivalently, this corresponds to higher fundamental wavenumber $k_x = 2\pi sk_\theta$.

However, at sufficiently large shear, eigenmodes may become strongly localized (as shown in Fig. 2). Figure 11a shows the convergence of Q_e with increasing radial wavenumber resolution at fixed radial box size L_x. At traditional ion-scale resolution, spurious levels of Q_e are found, such that the ion-scale Q_e is on the same order or larger than the electron-scale Q_e for $a/L_{Te} \leq 17$. Comparing with the multiscale simulation, this implies that the cross-scale coupling suppresses the MTM turbulence. However, as we mentioned previously, the reduction cannot be attributed to coupling with unstable ETG modes. In Fig. 11a, for the ion-scale simulation, we find that Q_e does not numerically converge until we reach *multiscale* radial resolution. This is required not for resolving the linearly unstable MTM, but rather the shorter-wavelength stable modes. There is a small stabilizing effect on the MTM turbulence from the $\mathbf{E}\times\mathbf{B}$ flow shear γ_E (see Table A1), where γ_E is the Waltz shearing rate [46]. For example, Q_e increases from 0.01 Q_{GB} to 0.2 Q_{GB} at the multiscale radial resolution when γ_E is set to zero. But this does not account for the overall very small fluxes. Even at this extreme radial resolution, though, the flux does not reproduce the transport at equivalent ion-scale binormal wavenumbers in the multiscale simulation. This is shown more clearly in Fig. 11b. Using the high (multiscale) radial resolution, as binormal wavenumber resolution increases toward the multiscale result, the high-k_θ ETG-driven flux grows. While the contribution to the total flux is small, coupling to unstable ETG modes increases the low-k_θ (MTM-driven) transport.

In this paper, we do not address the influence of global (profile shearing) effects on the MTMs. Global linear gyrokinetic simulations have been able to reproduce some distinctive features of experimentally observed fluctuations, such as magnetic frequency bands [47]. However, nonlinear global simulations can produce a well-known profile-flattening effect [48] (e.g. of the temperature gradient) and may spuriously lower the ion-scale turbulence levels even further. In the end, the result of our multiscale study is that, while the electron-scale simulation is valid for reproducing the electron transport levels, it is not possible to accurately simulate the MTM turbulence in this case with separable ion-scale simulations.

7. Summary

Multiscale gyrokinetic simulations of plasma turbulence for regimes of MTM and ETG-driven turbulence have been performed to study the validity of scale-separated simulations that resolve only ion or only electron spatio-temporal scales. The simulations were based on H-mode pedestal-like parameters from an NSTX experiment, where electromagnetic fluctuations are large. The linear analysis showed a dominant MTM at low (ion-gyro-radius-scale) binormal wavenumbers and dominant ETG modes at high (electron-gyroradius-scale) wavenumbers. The linear spectrum is separable in that no modes are linearly unstable at intermediate wavenumbers. Both of the single-scale (ion-scale and electron-scale) nonlinear simulations produce well-converged transport states. It was shown that saturation of electron-scale simulations does not require ion-scale zonal flows. Surprisingly, the multiscale electron transport closely follows the transport from the electron-scale simulations, implying a suppression of ion-scale MTM turbulence. The result is robust in a scan over electron temperature gradient, the key driver of ETG modes. At first glance, these results imply a suppression of MTM turbulence by ETG turbulence. However, the significantly reduced levels of MTM turbulence persist even when the high-k_θ turbulence is low, and thus cannot be attributed to ETG-coupling. Traditional ion-scale simulations

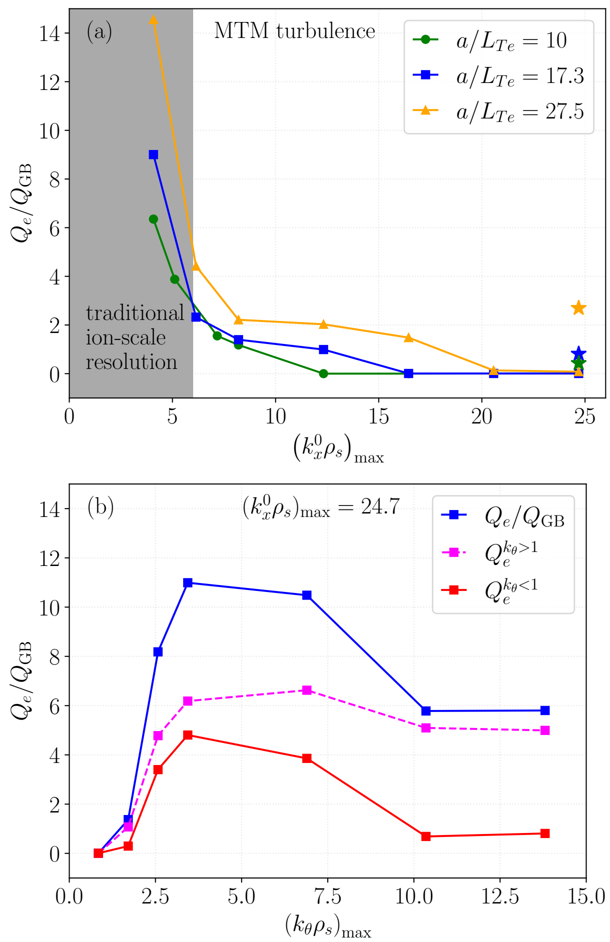

Figure 11. (a) Convergence of Q_e in ion-scale simulations of MTM turbulence with increasing radial wavenumber resolution (at fixed L_x). Spurious high levels of Q_e are found with traditional ion-scale radial resolution. Stars indicate the subcomponents of the fluxes containing only ion-scale wavenumbers ($0 < k_\theta\rho_s \leq 0.85$) from the full multiscale simulations. (b) Convergence of simulations with binormal resolution at fixed (multiscale) radial resolution. It is not possible to fully reproduce the transport at equivalent ion-scale wavenumbers in the multiscale simulation with ion-scale simulation.

generate spurious MTM turbulence that overestimates the electron energy flux. While the contribution of the MTM turbulence to the overall transport is small, the ion-scale simulations cannot fully reproduce the transport at the equivalent wavenumbers in the multiscale simulation. Overall, the results confirm the validity of the electron-scale simulations for predicting the electron transport in this case. However, they also indicate that separable ion-scale simulations may not be valid for simulating the MTM turbulence.

We caution that, from this analysis, we cannot generalize for which cases electron-scale simulations are expected to saturate and when ion-scale and electron-scale simulations can be added to accurately predict the turbulent fluxes. The only true test of the scale separation is to perform a multiscale simulation. Future work will expand multiscale analysis for a broader range of turbulence regimes, e.g. ETG with ion-scale turbulence dominated by ITG, TEM, and different classes of MTMs. Due to the high computational expense of multiscale simulation, further identification of the validity of the separability approximation for ion-scale and electron-scale turbulence is essential for developing reduced models and for practical integrated transport modeling.

Acknowledgments

We thank S. Kaye for helpful advice and discussion. This material is based upon work supported by the U.S. Department of Energy, Office of Science, Office of Fusion Energy Sciences under awards DE-FG02-95ER54309, DE-SC0024425 (FRONTIERS SciDAC-5 project), and DE-AC02-09CH11466/PPPL Field Work Proposal Number 3219 (CEDA SciDAC-5 project). An award of computer time was provided by the INCITE program. This research used resources of the Oak Ridge Leadership Computing Facility, which is an Office of Science User Facility supported under Contract DE-AC05-00OR22725. Computing resources were also provided by the National Energy Research Scientific Computing Center, which is an Office of Science User Facility supported under Contract DE-AC02-05CH11231. This report was prepared as an account of work sponsored by an agency of the United States Government. Neither the United States Government nor any agency thereof, nor any of their employees, makes any warranty, express or implied, or assumes any legal liability or responsibility for the accuracy, completeness, or usefulness of any information, apparatus, product, or process disclosed, or represents that its use would not infringe privately owned rights. Reference herein to any specific commercial product, process, or service by trade name, trademark, manufacturer, or otherwise, does not necessarily constitute or imply its endorsement, recommendation, or favoring by the United States Government or any agency thereof. The views and opinions of authors expressed herein do not necessarily state or reflect those of the United States Government or any agency thereof.

Appendix A. Simulation equilibrium parameters

The simulation equilibrium profile and geometry parameters based on NSTX #132588 at $t = 650$ ms for r/a=0.9 are given in Table A1 and Table A2, respectively.

Data Availability

The data that support the findings of this study are available from the corresponding author upon reasonable request.

References

[1] Applegate D, Roach C, Connor J, Cowley S, Dorland W, Hastie R and Joiner N 2007 *Plasma Phys. Control. Fusion* **49** 1113
[2] Guttenfelder W, Candy J, Kaye S, Nevins W, Wang E, Bell R, Hammett G, LeBlanc B, Mikkelsen D and Yuh H 2011 *Phys. Rev. Lett.* **106** 155004
[3] Giacomin M, Dickinson D, Patel B and Roach C 2023 *Plasma Phys. Control. Fusion* **65** 095019
[4] Ding S and Garofalo A 2023 *Rev. Mod. Phys.* **7** 4
[5] Viezzer E, Cavedon M, Fable E, Laggner F, McDermott R, Galdon-Quiroga J, Dunne M, Kappatou A, Angioni C, Cano-Megias P, Cruz-Zabala D, Dux R, Pütterich T, Ryter F,

Table A1. Simulation equilibrium pedestal profile parameters based on NSTX #132588. Note that $x \doteq r/a$, where r is the midplane minor radius and a is the minor radius of the last closed flux surface.

Parameter	Description	Value
r/a	minor radius	0.9
n_i/n_e	ion density	1.0
T_i/T_e	ion temperature	1.86
a/L_{ne}	$-(d/dx)\ln n_e$	7.0
a/L_{ni}	$-(d/dx)\ln n_i$	7.0
a/L_{Te}	$-(d/dx)\ln T_e$	17.3
a/L_{Ti}	$-(d/dx)\ln T_i$	3.9
$\beta_{e,\mathrm{unit}}$	$8\pi n_e T_e/B^2_{\mathrm{unit}}$	1.82 $\times 10^{-3}$
$(a/c_s)\nu_{ee}$	electron collision rate	1.34
M	ion sound Mach num	0.0
$(a/c_s)\gamma_p$	toroidal rotation shear	0.0
$(a/c_s)\gamma_E$	$\mathbf{E}\times\mathbf{B}$ flow shear	0.21
λ_*	Debye length	0.014

Table A2. Simulation equilibrium geometry parameters based on NSTX #132588, including the major radius R_0, safety factor q, shear s, elongation κ, triangularity δ, squareness ζ, and symmetric shaping parameter s_3 [32].

Parameter	Value	Parameter	Value
R_0/a	1.49	dR_0/dr	-0.585
Z_0/a	-0.223	dZ_0/sr	-0.197
q	5.45	s	4.56
κ	2.1846	s_κ	-0.1831
δ	0.3678	s_δ	0.3186
ζ	0.0287	s_ζ	0.1008
s_3	0.0052	$(d/dx)s_3$	-0.0428
s_4	0.0089	$(d/dx)s_4$	-0.0006
s_5	0.0074	$(d/dx)s_5$	0.0163
c_0	-0.0351	$(d/dx)c_0$	-0.0612
c_1	-0.0410	$(d/dx)c_1$	-0.0573
c_2	0.0088	$(d/dx)c_2$	0.0427
c_3	-0.0018	$(d/dx)c_3$	-0.0017
c_4	-0.0067	$(d/dx)c_4$	-0.0099
c_5	-0.0045	$(d/dx)c_5$	0.0142

Wolfrum E, the ASDEX Upgrade Team and the EUROfusion MST1 Team 2018 *Nucl. Fusion* **58** 026031

[6] Haskey S, Ashourvan A, Banerjee S, Barada K, Belli E, Bortolon A, Candy J, Chen J, Chrystal C, Grierson B, Groebner R, Laggner F, Knolker M, Kramer G, Major M, Mckee G, Staebler G, Yan Z and Zeeland M V 2022 *Phys. Plasmas* **29** 012506

[7] Hatch D, Told D, Jenko F, Doerk H, Dunne M, Wolfrum E, Viezzer E, the ASDEX Upgrade Team and Pueschel M 2015 *Nucl. Fusion* **55** 063028

[8] Kotschenreuther M, Hatch D, Mahajan S, Valanju P, Zheng L and Liu X 2017 *Nucl. Fusion* **57** 064001

[9] Kotschenreuther M, Liu X, Hatch D, Mahajan S, Zheng L, Diallo A, Groebner R, the DIII-D Team, Hillesheim J, Maggi C, Giroud C, Koechl F, Parail V, Saarelma S, Solano E, Chankin A and JET Contributors 2019 *Nucl. Fusion* **59** 096001

[10] Guttenfelder W, Groebner R, Canik J, Grierson B, Belli E and Candy J 2021 *Nucl. Fusion* **61** 056005

[11] Hatch D, Kotschenreuther M, Mahajan S, Valanju P, Jenko F, Told D, Görler T and Saarelma S 2016 *Nucl. Fusion* **56** 104003

[12] Hatch D, Kotschenreuther M, Mahajan S, Valanju P and Liu X 2017 *Nucl. Fusion* **57** 036020

[13] Guttenfelder W, Candy J, Kaye S, Nevins W, Wang E, Zhang J, Bell R, Crocker N, Hammett G, LeBlanc B, Mikkelsen D and Yuh Y R H 2012 *Phys. Plasmas* **19** 056119

[14] Giacomin M, Kennedy D, Casson F, Ajay C, Dickinson D, Patel B and Roach C 2024 *Plasma Phys. Control. Fusion* **66** 055010

[15] Candy J 2005 *Phys. Plasmas* **12** 072307

[16] Waltz R 2010 *Phys. Plasmas* **17** 072501

[17] Pueschel M, Terry P, Jenko F, Hatch D, Nevins W, Gorler T and Told D 2013 *Phys. Rev. Lett.* **110** 155005

[18] Candy J, Waltz R, Fahey M and Holland C 2007 *Plasma Phys. Control. Fusion* **49** 1209

[19] Maeyama S, Idomura Y, Watanabe T H, Nakata M, Yagi M, Miyato N, Ishizawa A and Nunami M 2015 *Phys. Rev. Lett.* **114** 255002

[20] Howard N, Holland C, White A, Greenwald M, Candy J and Creely A 2016 *Phys. Plasmas* **23** 056109

[21] Holland C, Howard N and Grierson B 2017 *Nucl. Fusion* **57** 066043

[22] Maeyama S, Howard N, Citrin J, Watanabe T H and Tokuzawa T 2024 *Nucl. Fusion* **64** 112007

[23] Belli E, Candy J and Sfiligoi I 2023 *Plasma Phys. Control. Fusion* **65** 024001

[24] Belli E, Candy J and Sfiligoi I 2024 *Plasma Phys. Control. Fusion* **66** 045019

[25] Maeyama S, Watanabe T H, Idomura Y, Nakata M, Ishizawa A and Nunami M 2017 *Phys. Rev. Lett.* **119** 195002

[26] Maingi R, Osborne T, Bell M, Bell R, Boyle D, Canik J, Diallo A, Kaita R, Kaye S, Kugel H, LeBlanc B, Sabbagh S, Skinner C, Soukhanovskii V and the NSTX Team 2015 *J. Nucl. Mater.* **463** 1134

[27] Guttenfelder W, Battaglia D, Diallo A, Maingi R, Kaye S, Parisi J, Dorland W, Gaur R, Canik J, Belli E and Candy J 2022 *Bull. Am. Phys. Soc.* **PI01.00001**

[28] Dominski J, Guttenfelder W, Hatch D, Goerler T, Jenko F, Munaretto S and Kaye S 2024 *Phys. Plasmas* **31** 044501

[29] Candy J, Belli E and Bravenec R 2016 *J. Comput. Phys.* **324** 73

[30] Candy J, Sfiligoi I, Belli E, Hallatschek K, Holland C, Howard N and ED'Azevedo 2019 *Computers & Fluids* **188** 125

[31] Sfiligoi I, Belli E, Candy J, and Budiardja R 2023 *In PEARC '23: Practice and Experience in Advanced Research Computing, Association for Computing Machinery* 246-250

[32] Arbon R, Candy J and Belli E 2021 *Plasma Phys. Control. Fusion* **63** 012001

[33] Sugama H, Watanabe T H and Nunami M 2009 *Phys. Plasmas* **16** 112503

[34] Candy J 2009 *Plasma Phys. Control. Fusion* **51** 105009

[35] Belli E and Candy J 2008 *Plasma Phys. Control. Fusion* **50** 095010

[36] Belli E and Candy J 2012 *Plasma Phys. Control. Fusion* **54** 015015

[37] Beer M 1995 *Gyrofluid Models of Turbulent Transport in Tokamaks* Ph.D. thesis Princeton University

[38] Candy J, Waltz R and Rosenbluth M 2004 *Phys. Plasmas* **11** 1879

[39] Told D, Jenko F, Xanthopoulos P, Horton L, Wolfrum E and ASDEX Upgrade Team 2008 *Phys. Plasmas* **15** 102306

[40] Parisi J, Parra F, Roach C, Giroud C, Dorland W, Hatch D, Barnes M, Hillesheim J, Aiba N, Ball J, Ivanov P and JET contributors 2020 *Nucl. Fusion* **60** 126045

[41] Chapman-Oplopoiou B, Hatch D, Field A, Frassinetti L, Hillesheim J, Horvath L, Maggi C, Parisi J, Roach C, Saarelma S, Walker J and JET Contributors 2020 *Nucl. Fusion* **62** 086028

[42] Hinton F, Rosenbluth M and Waltz R 2003 *Phys. Plasmas* **10** 168

[43] Staebler G, Howard N, Candy J and Holland C 2017 *Nucl. Fusion* **57** 066046

[44] Creely A J, Rodriguez-Fernandez P, Conway G D, Freethy S J, Howard N T, White A E and the ASDEX Upgrade Team 2019 *Plasma Phys. Control. Fusion* **61** 085022

[45] Pueschel M, Hatch D, Kotschenreuther M, Ishizawa A and Merlo G 2020 *Nucl. Fusion* **60** 124005

[46] Waltz R, Kerbel G and Milovich J 1994 *Phys. Plasmas* **1** 2229

[47] Hatch D, Kotschenreuther M, Mahajan S, Pueschel M, Michoski C, Merlo G, Hassan E, Field A, Frassinetti L, Giroud C, Hillesheim J, Maggi C, von Thun C P, Roach C, Saarelma S, Jarema

D, Jenko F and JET Contributors 2021 *Nucl. Fusion* **61** 036015
[48] Waltz R, Candy J and Rosenbluth M 2002 *Phys. Plasmas* **9** 1938